TU Delft

Delft University of Technology

Creation of memory–memory entanglement in a metropolitan quantum network

Liu, Jian-Long; Luo, Xi-Yu; Yu, Yong; Wang, Chao-Yang; Wang, Bin; Hu, Yi; Li, Jun; Bao, Xiao-Hui; Pan, Jian-Wei; More Authors

DOI
10.1038/s41586-024-07308-0

Publication date
2024

Document Version
Final published version

Published in
Nature

Citation (APA)
Liu, J.-L., Luo, X.-Y., Yu, Y., Wang, C.-Y., Wang, B., Hu, Y., Li, J., Bao, X.-H., Pan, J.-W., & More Authors (2024). Creation of memory–memory entanglement in a metropolitan quantum network. *Nature*, *629*, 579-585. https://doi.org/10.1038/s41586-024-07308-0

Important note
To cite this publication, please use the final published version (if applicable).
Please check the document version above.

Copyright
Other than for strictly personal use, it is not permitted to download, forward or distribute the text or part of it, without the consent of the author(s) and/or copyright holder(s), unless the work is under an open content license such as Creative Commons.

Takedown policy
Please contact us and provide details if you believe this document breaches copyrights.
We will remove access to the work immediately and investigate your claim.

This work is downloaded from Delft University of Technology.
For technical reasons the number of authors shown on this cover page is limited to a maximum of 10.

Green Open Access added to TU Delft Institutional Repository

'You share, we take care!' - Taverne project

https://www.openaccess.nl/en/you-share-we-take-care

Otherwise as indicated in the copyright section: the publisher is the copyright holder of this work and the author uses the Dutch legislation to make this work public.

Article

Creation of memory–memory entanglement in a metropolitan quantum network

https://doi.org/10.1038/s41586-024-07308-0

Received: 10 October 2023

Accepted: 13 March 2024

Published online: 15 May 2024

Check for updates

Jian-Long Liu[1,2,3,9], Xi-Yu Luo[1,2,3,9], Yong Yu[1,2,3,8,9], Chao-Yang Wang[1,2,3], Bin Wang[1,2,3], Yi Hu[1,2,3], Jun Li[1,2,3], Ming-Yang Zheng[4], Bo Yao[5,6], Zi Yan[1,2,3], Da Teng[1,2,3], Jin-Wei Jiang[1,2,3], Xiao-Bing Liu[5,6], Xiu-Ping Xie[4], Jun Zhang[1,2,3], Qing-He Mao[5,6,7], Xiao Jiang[1,2,3], Qiang Zhang[1,2,3,4], Xiao-Hui Bao[1,2,3]✉ & Jian-Wei Pan[1,2,3]✉

Towards realizing the future quantum internet[1,2], a pivotal milestone entails the transition from two-node proof-of-principle experiments conducted in laboratories to comprehensive multi-node set-ups on large scales. Here we report the creation of memory–memory entanglement in a multi-node quantum network over a metropolitan area. We use three independent memory nodes, each of which is equipped with an atomic ensemble quantum memory[3] that has telecom conversion, together with a photonic server where detection of a single photon heralds the success of entanglement generation. The memory nodes are maximally separated apart for 12.5 kilometres. We actively stabilize the phase variance owing to fibre links and control lasers. We demonstrate concurrent entanglement generation between any two memory nodes. The memory lifetime is longer than the round-trip communication time. Our work provides a metropolitan-scale testbed for the evaluation and exploration of multi-node quantum network protocols and starts a stage of quantum internet research.

Quantum networks[1,2] operate differently to their classical counterparts, as their nodes can store and process quantum information and are linked through the sharing of entangled states. The non-local nature of entanglement enables a range of disruptive applications such as quantum cryptography[4], distributed quantum computing[5] and enhanced sensing[6,7]. Quantum nodes within a metropolitan area can be entangled through optical channels of a few tens of kilometres with a moderate transmission loss (for example, 10 dB for 50-km fibre at 1,550 nm). For entangling intercity nodes, quantum repeater protocols[3,8] need to be implemented to overcome the exponential growth in transmission loss. Figure 1a shows an envisaged wide-area complex quantum network, consisting of a number of high-connectivity metropolitan-area networks that are further interconnected via quantum repeater channels.

The building block of a quantum network is the heralded entanglement between a pair of adjacent quantum nodes. This has been successfully demonstrated across various physical platforms including atomic ensembles[9–11], single atoms[12], diamond nitrogen-vacancy centres[13–15], trapped ions[16], rare-earth-doped crystals[17,18] and quantum dots[19,20], among others. Currently, the maximum physical separation of heralded entanglement achieved is 1.3 km (ref. 14). Building on this progress, three-node quantum network primitives have been established recently on a laboratory scale[21–23], opening opportunities for multi-user applications, such as the creation of three-body entangled Greenberger–Horne–Zeilinger (GHZ) states[21,22], entanglement swapping between two elementary links[22] and qubit teleportation between non-neighbouring nodes[23]. The next challenge is to extend these laboratory or short-scale experiments to a metropolitan scale, which needs the combination of several requirements: low fibre transmission loss, independent quantum nodes and a scalable network architecture. Owing to the great progress of the quantum frequency conversion (QFC) technique[24], platforms operating at high-transmission-loss wavelengths are now able to access the fibre network with minimal loss. This has enabled a series of works distributing local light–matter entanglement over up to a few-kilometre fibres[25–30]. Furthermore, two seminal experiments demonstrated heralded entanglement between two quantum nodes via long fibre links, one using two single atoms and 33 km of fibre[31] and the other using two atomic ensembles and 50 km of fibre[32]. However, the entanglement between two single atoms was generated at a low rate of approximately 1 min^{-1} and the entanglement between two atomic ensembles was generated between two non-independent nodes, raising concerns about their scalability towards large-scale and multi-user scenarios.

Here we overcome these challenges with a set of key innovations and present a multi-node quantum network over a metropolitan area. Our network consists of three quantum nodes (Alice, Bob and Charlie) and a server node arranged in a star topology (Fig. 1d). The three quantum nodes are located on the three vertices of a triangle with sides of 7.9 km to 12.5 km in length in Hefei city, and run independently.

[1]Hefei National Research Center for Physical Sciences at the Microscale and School of Physical Sciences, University of Science and Technology of China, Hefei, China. [2]CAS Center for Excellence in Quantum Information and Quantum Physics, University of Science and Technology of China, Hefei, China. [3]Hefei National Laboratory, University of Science and Technology of China, Hefei, China. [4]Jinan Institute of Quantum Technology, Jinan, China. [5]Anhui Provincial Key Laboratory of Photonics Devices and Materials, Anhui Institute of Optical and Fine Mechanics, Hefei Institutes of Physical Science, Chinese Academy of Science, Hefei, China. [6]Advanced Laser Technology Laboratory of Anhui Province, Hefei, China. [7]School of Environmental Science and Optoelectronic Technology, University of Science and Technology of China, Hefei, China. [8]Present address: Kavli Institute of Nanoscience, Delft University of Technology, Delft, The Netherlands. [9]These authors contributed equally: Jian-Long Liu, Xi-Yu Luo, Yong Yu. ✉e-mail: xhbao@ustc.edu.cn; pan@ustc.edu.cn

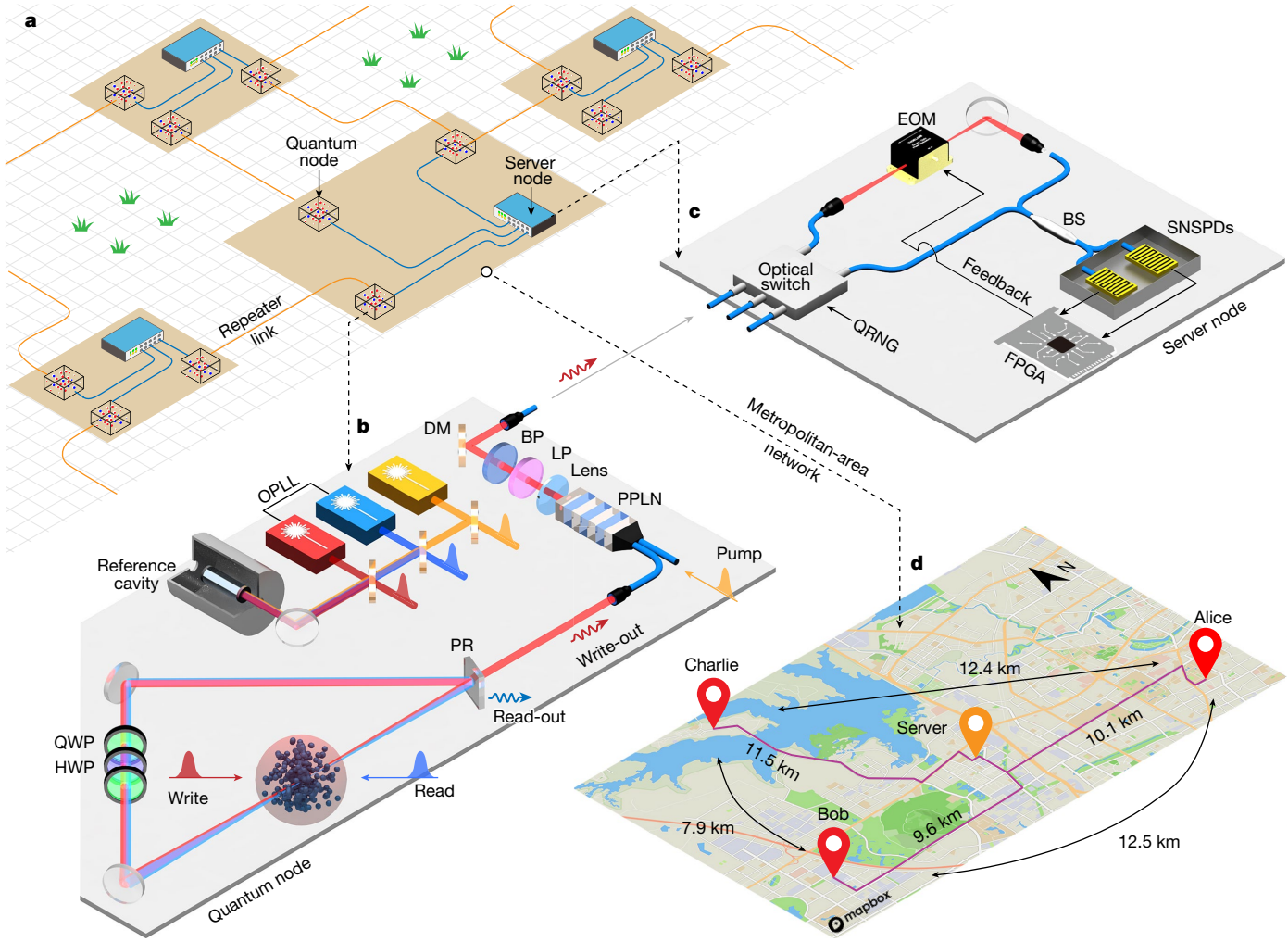

Fig. 1 | Network layout and experimental set-up. a, An envisaged architecture of a wide-area quantum network. Most of the quantum nodes are located in metropolitan areas (shaded in brown), forming numerous metropolitan-area networks. Each metropolitan area has a server node that connects and synchronizes all quantum nodes, facilitating remote entanglement generation between any pair of quantum nodes on request. Quantum nodes in different cities establish remote entanglement through quantum repeater links (orange lines) that connect the metropolitan-area networks. **b**, Scheme of the quantum node. A cloud of ^{87}Rb atoms in a ring cavity works as a quantum memory, and the atom–photon entanglement is generated with the DLCZ protocol. The write-out photon, emitted through a partially reflective (PR) mirror, is shifted to the telecom wavelength with a QFC module and then sent to the server node. The dichroic mirrors (DMs), long-pass filters (LPs) and bandpass filters (BPs) are used for noise filtering in the conversion process. All lasers are locked to a reference cavity. The write and read lasers are furthermore synchronized using an OPLL. PPLN, periodically poled lithium niobate; QWP, quarter-wave plate; HWP, half-wave plate. **c**, Scheme of the server node. An optical switch controlled by a QRNG routes two of the three inputs to the interferometer. A beamsplitter (BS) performs single-photon interference and the results are measured by two SNSPDs. A field-programmable gate array (FPGA) is used to analyse the phase-probe interference data and compensate the phase to the electro-optical modulator (EOM) on one arm of the interferometer (see main text). **d**, Layout of the multi-node quantum network studied in this work. Three quantum nodes, labelled Alice, Bob and Charlie, and a server node are located in four laboratories in the Hefei city. The violet lines represent the fibre connections (lengths indicated) and the black arrows indicate the physical distance between quantum nodes. Map data from Mapbox and OpenStreetMap.

The server node is situated approximately in the centre of the triangle and linked to each quantum node via optical fibres for both classical and quantum communication. In each quantum node, a cavity-enhanced laser-cooled rubidium atomic ensemble serves as the long-lived quantum memory[33], generating atom–photon entanglement using the Duan–Lukin–Cirac–Zoller (DLCZ) protocol[34]. The photon is sent to the server node for entangling, while the atomic qubit is stored for subsequent applications. To reduce photon loss in the fibre, each quantum node is equipped with a QFC module, which coherently shifts visible photons at the rubidium resonance to the telecom O band[32]. Quantum nodes are furthermore synchronized in phase using a remote phase-stabilization method. Using this architecture, we demonstrated the generation of entanglement between distant quantum nodes and the storage of entanglement exceeding the round-trip communication time. Furthermore, we extended the remote entanglement generation to all three links in the network and executed them concurrently.

Scheme and experimental set-up

We generate remote entanglement between a pair of distant quantum nodes via a single-photon scheme[34]. We start by preparing the light–matter entanglement in each quantum node (Fig. 1b) using the DLCZ protocol[34]. A weak write pulse induces a spontaneous Raman-scattered photon (write-out) with a small probability $\chi \approx 1\%$, whose presence and absence is associated with that of collective excitation of the atomic ensemble. This forms a Fock-basis light–matter entanglement $|\Phi_{ap}\rangle = |00\rangle + \sqrt{\chi}\,|11\rangle$ without normalization, where the subscript 'a'

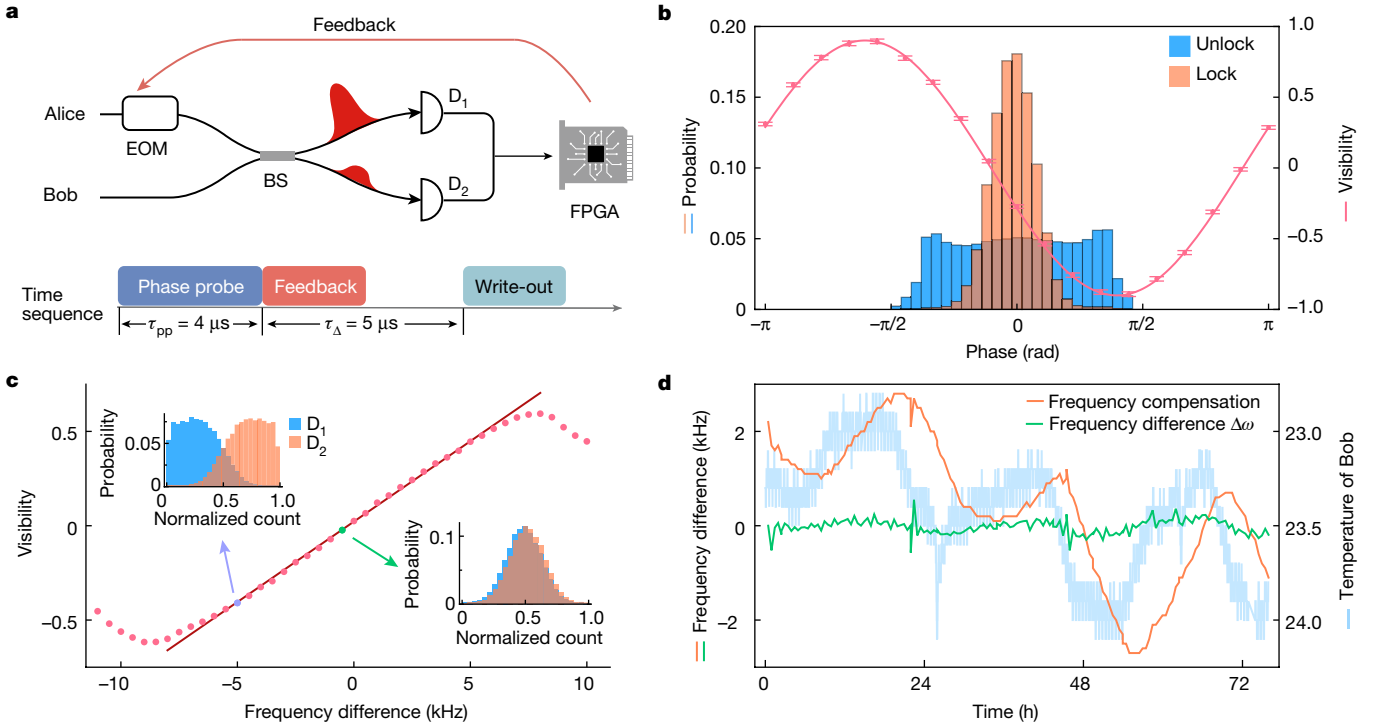

Fig. 2 | Weak-field phase and frequency stabilization. a, Schematic and time sequence of the phase-stabilization method. We probe the phase difference of two nodes by interfering two phase-probe pulses on the entanglement generation facilities. An FPGA extracts the phase difference and applies the feedback to the EOM. In each trial, phase-probe pulses are sent before the write process, and a gap of $\tau_\Delta = 5$ μs is secured to reduce the afterpulse-like noise of the SNSPDs. Each phase-probe pulse lasts for $\tau_{pp} = 4$ μs and contains about 40 photons upon arrival at the beamsplitter. The feedback takes up to 2 μs. In practice, the probe-feedback process is executed twice for better phase-stabilization performance. **b**, Characterization of phase stabilization. The two histograms show the detected phase distributions with (orange) and without (blue) executing the phase stabilization. When running the phase stabilization, we perform single-photon interference by sending weak pulses from two nodes. The pink data points show the interference visibility as a function of their phase difference. The pink curve is a sinusoidal fitting of the data points. The error bars represent one standard deviation. **c**, Interference visibility of phase-probe pulses as a function of the frequency difference between two nodes. The pink data points show the variation in visibility when deliberately changing the frequency difference. The red line is a linear fitting of the data points within ±5 kHz. The two histograms in the insets show the distribution of the counts of two SNSPDs (D_1 and D_2) within a 120-s timeslot, with the corresponding data points highlighted. **d**, Tracking of laser drift over 76 hours. The green curve shows the detected frequency difference after compensation. The orange curve shows the compensation value, which approximates the original laser drift. We plot the temperature of Bob in blue, which shows a strong correlation with the laser drift.

denotes the atomic state in the first part, the subscript 'p' denotes the photonic state in the second part, and 0 and 1 refer to the number of atomic or photonic excitations. The atomic excitation can be stored for up to 560 μs until it is retrieved for following operations[30]. The write-out photon is down-converted from 795 nm at rubidium resonance to 1,342 nm in the telecom O band in a periodically-poled-lithium-niobate waveguide chip with the help of a strong 1,950-nm pump laser. The photon attenuation is thus reduced from 3.5 dB km^{-1} to 0.3 dB km^{-1} under transmission through standard optical fibres (see Supplementary Information for measured attenuation in our experiments). The telecom photon then is sent to the server node for interference. The QFC module, including the down-conversion, noise filtering and fibre coupling, constitute an end-to-end efficiency of 46% and noise of about 1.3 kHz. In the server node (Fig. 1c), a beamsplitter combines the write-out photon from two quantum nodes and erases their which-path information. A click from a superconducting nanowire single-photon detector (SNSPD) heralds the maximally entangled states between two ensembles

$$|\Psi_{aa}^{\pm}\rangle = (|01\rangle \pm e^{i\Delta\varphi}\,|10\rangle)/\sqrt{2}, \quad (1)$$

where the ± sign depends on the heralding detector. $\Delta\varphi = \Delta\varphi_w + \Delta\varphi_p + \Delta\varphi_f$ accounts for the optical phase difference accumulated during the entangling process, including $\Delta\varphi_w$ and $\Delta\varphi_p$, the phase difference of write lasers and of pump lasers in two nodes, respectively, as well as $\Delta\varphi_f$, the phase difference of two fibre channels.

The key to the success of the single-photon scheme lies in accurately setting $\Delta\varphi$ to a known value. To this end, previous laboratory experiments have typically used an ad hoc laser shared by separated nodes, and locked the closed-loop interferometer composed of the laser splitting paths and the quantum channels[9,17,20,22,32]. In addition, the qubit manipulation laser paths typically do not coincide with the laser splitting paths, so these two paths should also be locked to maintain the coherence of the quantum states, which further adds the phase-locking complexity[22].

To address these challenges, we developed a network architecture based on a weak-field remote phase-stabilization method. The method relies on detecting the phase difference $\Delta\varphi$ in situ at the entanglement generation facilities using weak-field phase-probe pulses and photon counting, and compensating for it immediately (see Fig. 2a for the scheme and more details in Supplementary Information), similar to that realized recently in quantum key distribution experiments[35]. This method has three critical requirements for the phase-probe pulses: their frequency difference is much smaller than $1/\tau_{pp}$ (where τ_{pp} is the phase probe time), their linewidths are much narrower than $1/\tau_{pp}$ and $1/\tau_\Delta$ (where τ_Δ is the time gap between the phase probe and the write process), and they inherit the same laser phase as the write-out photons. To meet these requirements, we lock all lasers in each node

onto a reference cavity and obtain a subkilohertz linewidth and drift of a few kilohertz per day for all lasers. We perform a one-off frequency calibration of the corresponding lasers in different nodes. In addition, we synchronize the write and read lasers using an optical phase-locked loop (OPLL). As a result, each phase-probe pulse differs from the corresponding write-out photon with a phase θ, leading to a residual phase $\Delta\theta$ (the difference of θ in two nodes) in equation (1) after compensation. One can either remove $\Delta\theta$ by synchronizing the OPLLs in two nodes or choose $\Delta\theta$ as the phase reference to observe the entanglement. We choose the latter method in the following experiments.

To characterize the stabilization performance, we send an additional phase-probe pulse from each quantum node 5 μs after the feedback and find a Gaussian phase distribution with a standard deviation of 17°, as shown in Fig. 2b. By changing the relative phase between the additional pair of phase-probe pulses, we observe a sinusoidal oscillation of their interference visibility (Fig. 2b), which confirms a good phase correlation between two nodes.

An additional challenge in operations arises from the slow frequency drift of the reference cavities, which can transfer to the lasers and eventually to write-out photons. To avoid this, we use a continuous frequency calibration using the phase-probe interference data. We determine the minor laser frequency offset $\Delta\omega$ by analysing the phase evolution between successive entanglement trials over a duration of t and compensate it to the pump lasers. Considering the long coherence time of the lasers (about 1 ms) and the slow fluctuations in the fibre, the phase evolves solely owing to $\Delta\omega t$. We verify this by observing the interference visibility as a function of $\Delta\omega$, shown in Fig. 2c. Through the implementation of the calibration, we are able to maintain $\Delta\omega \leq 0.15$ kHz over a span of 76 h, despite an observed drift of 5 kHz (Fig. 2d).

Entanglement between a pair of distant nodes

We first generate remote entanglement between Alice and Bob. The atomic qubits are encoded in the Fock basis of excitations, and are difficult to measure directly without introducing interactions[36]. Instead we retrieve each atomic state to a photonic mode[3] and obtain $|\Psi^{\pm}_{\mathrm{pp}}\rangle = (|01\rangle \pm \mathrm{e}^{\mathrm{i}\Delta\varphi_{\mathrm{r}}}|10\rangle)/\sqrt{2}$. To evaluate the photonic entanglement, one needs the knowledge of coherence $d \equiv |\langle 10|\Psi^{\pm}_{\mathrm{pp}}\rangle\langle\Psi^{\pm}_{\mathrm{pp}}|01\rangle|$. As it is experimentally hard to perform qubit operations in the Fock basis, previous experiments mostly inferred d by interfering two read-out modes using a beamsplitter[9,17,32], which is not favourable for spatially separate cases. To overcome this challenge, we develop a method based on the weak-field homodyne measurement schemes[37,38] that allows us to witness remote Fock-basis entanglement through local operations and measurements. In addition, our method effectively converts the Fock-basis entanglement into a polarization maximally entangled (PME) state[34], making it accessible for entanglement-based communication schemes.

Our method starts by generating an entanglement-probe pulse from the write laser in each node. It is a weak coherent light field that has the same frequency and profile (confirmed by the Hong–Ou–Mandel experiment between the entanglement-probe pulse and the read-out field in Fig. 3b) as the read-out field, but orthogonally polarized. When choosing the phase reference of $\mathrm{e}^{\mathrm{i}\Delta\theta}$, one can find the joint state of two entanglement-probe pulses $|\mathrm{EP}\rangle_{\mathrm{A}}|\mathrm{EP}\rangle_{\mathrm{B}} \approx |00\rangle + \alpha(|01\rangle + \mathrm{e}^{\mathrm{i}\Delta\varphi_{\mathrm{r}}}|10\rangle)$, where α is the amplitude of the entanglement-probe (EP) pulse, is in phase with $|\Psi^{\pm}_{\mathrm{pp}}\rangle$. Next, we combine the read-out field with the entanglement-probe pulse in every node using a polarizing beamsplitter (PBS) and perform projection measurements under different polarization bases (Fig. 3a). Initially, we measure the mixed field in both nodes in the $|H\rangle/|V\rangle$ basis, where H and V stand for the light field's horizontal and vertical polarization modes, respectively. On the detector corresponding to horizontal polarization, the entanglement-probe pulse is removed; thus we find p_{00}, p_{01}, p_{10} and p_{11} through statistical analysis, where p_{ij} represents the probability of having i excitations in Alice and j excitations in Bob. When measuring in the superposition basis, the read-out field interferes with the entanglement-probe pulses, resulting in remote correlation. Specifically, when the $|H\rangle \pm |V\rangle$ basis is chosen, we have the correlation function

$$E_{\pm} = \frac{N_{++} + N_{--} - N_{+-} - N_{-+}}{N_{++} + N_{--} + N_{+-} + N_{-+}}, \tag{2}$$

where N_{mn} represents the coincidence events between the m mode in Alice and the n mode in Bob (m, n takes + or −, referring to $|H\rangle + |V\rangle$ and $|H\rangle - |V\rangle$, respectively). In this case, we find $|d| > (p_{01} + p_{10} + 2\sqrt{p_{00}p_{11}})|E_{\pm}|/2$ (Supplementary Information). Now we can estimate the degree of entanglement with the lower bound of concurrence $\mathcal{C} = \max(0, 2|d| - 2\sqrt{p_{00}p_{11}})$. This measure ranges from 0 for a separable state to 1 for a maximally entangled state.

Although being a good measure of entanglement, $\mathcal{C}$ does not indicate how useful the entangled state is in entanglement-based communication. To answer this question, we consider the mixed field right after the combining PBS at each node, which can be approximated (with arbitrary phase factors and no normalization)

$$(a^{\dagger}_{\mathrm{A},H} \pm a^{\dagger}_{\mathrm{B},H}) \otimes (\mathbb{1} + \alpha a^{\dagger}_{\mathrm{A},V}) \otimes (\mathbb{1} + \alpha a^{\dagger}_{\mathrm{B},V})|0\rangle, \tag{3}$$

where $\mathbb{1}$ is the identity operator and $a^{\dagger}$ is the photon creation operator with the subscript indicating its node (Alice or Bob) and polarization (H or V). Selecting at least one photon at each node, equation (3) becomes

$$|\Psi^{\pm}_{\mathrm{PME}}\rangle = \alpha(a^{\dagger}_{\mathrm{A},H}a^{\dagger}_{\mathrm{B},V} \pm a^{\dagger}_{\mathrm{A},V}a^{\dagger}_{\mathrm{B},H})\ |0\rangle + o(\alpha^2). \tag{4}$$

Neglecting the higher-order term $o(\alpha^2)$, equation (4) is a PME state between two photonic modes. This allows local Pauli operations (X, Y and Z) and enables entanglement-based communication protocols. More details about the weak-field entanglement verification method are discussed in Supplementary Information.

Next, we verify the remote entanglement generated between Alice and Bob using the weak-field method. In the first experiment, we verify the entanglement in a delayed-choice fashion[39]. The atomic states are retrieved 5 μs after the atom–photon entanglement is created, earlier than the entanglement is heralded. Figure 3c,d summarizes the reconstructed density matrices between the read-out fields and the corresponding $\mathcal{C}$. $\mathcal{C} > 0$ for both $|\Psi^{+}_{\mathrm{pp}}\rangle$ and $|\Psi^{-}_{\mathrm{pp}}\rangle$ indicates the existence of remote entanglement. By deducting the loss during retrieval and detection, we infer the density matrices between two atomic ensembles and their corresponding concurrence $\tilde{\mathcal{C}}$ to two atomic ensembles and show them in the same figures. Meanwhile, we find the fidelity $\mathcal{F} = 0.672(32)$ for $|\Psi^{+}_{\mathrm{PME}}\rangle$ and $\mathcal{F} = 0.666(31)$ for $|\Psi^{-}_{\mathrm{PME}}\rangle$ to the corresponding maximally entangled state, both above 0.5 to certify the entanglement (Fig. 3e,h). In the second experiment, we create the remote entanglement in the same fashion but store it for 107 μs, exceeding the round-trip transmission time between the quantum and the server nodes. We get a slightly lower concurrence result for each case, as summarized in Fig. 3f,g. In terms of fidelities, we get $\mathcal{F} = 0.643(40)$ for $|\Psi^{+}_{\mathrm{PME}}\rangle$ and $\mathcal{F} = 0.637(40)$ for $|\Psi^{-}_{\mathrm{PME}}\rangle$, which are on par with that of the former experiment (Fig. 3e,h). Comparing the variation of $\mathcal{C}$ and $\mathcal{F}$ between the two experiments, we confirm that a large portion of noise in the generated entangled states is the vacuum component and can be effectively filtered out using our weak-field method and other protocols[34]. The measured heralding probability is 6.9×10^{-4} and 8.0×10^{-4} for the first and second experiments, respectively, which corresponds to an entangling rate of 1.93 Hz and 0.83 Hz, considering the experiment repetition rate of 2.76 kHz and 1.03 kHz. In both experiments, 25% of the heralding events come from the dark counts or the noise photons, and the left part comes

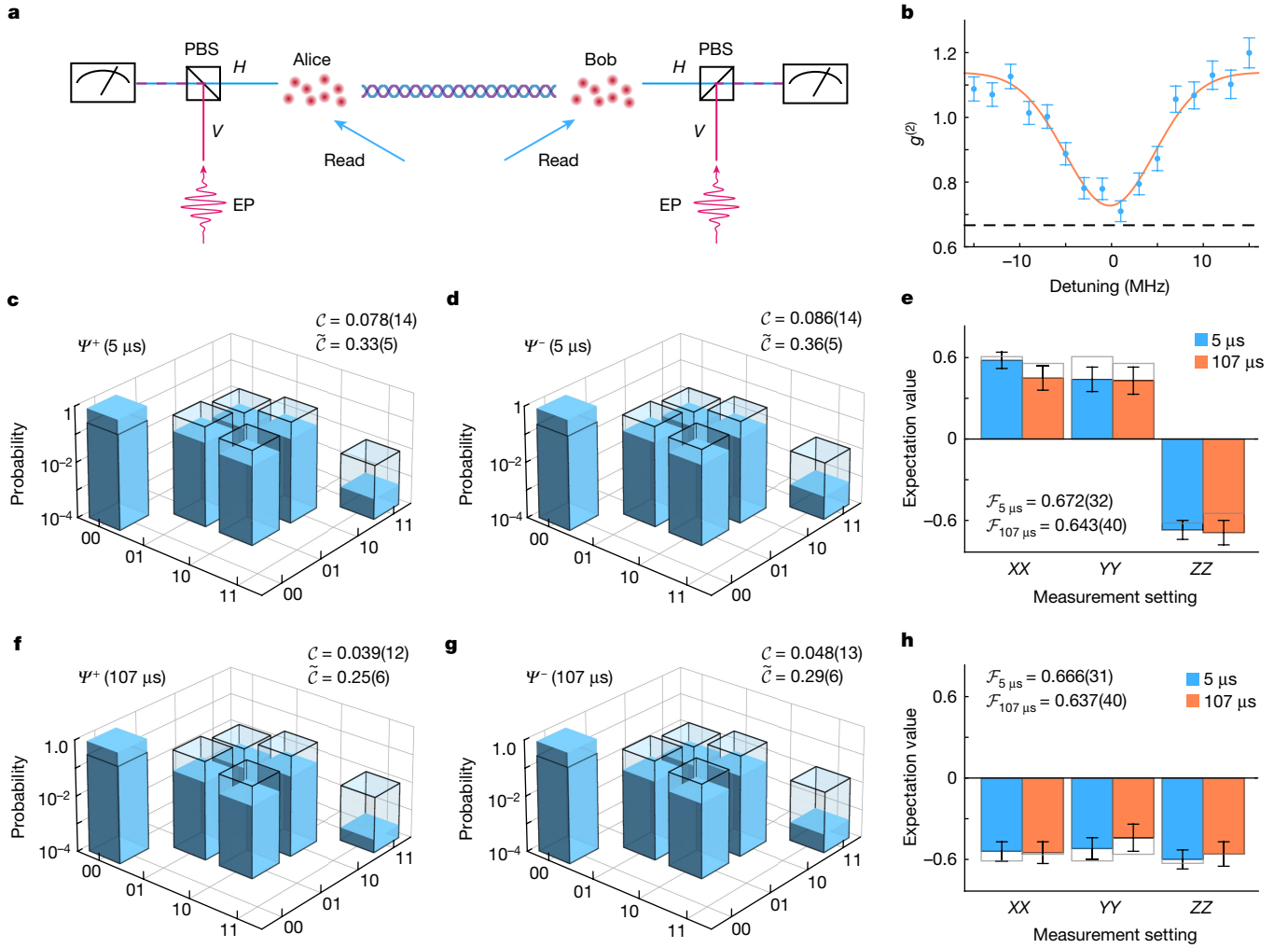

Fig. 3 | Entanglement between a pair of distant nodes. a, The experimental set-up for entanglement verification. In each node, a weak entanglement-probe (EP) pulse that has the same frequency and profile as the read-out field but is orthogonally polarized assists in the verification process. We combine the entanglement-probe pulses and the read-out fields using PBSs, perform the polarization measurement in each node, and detect the remote entanglement by analysing the correlation between two nodes (see main text). **b**, Measured correlation function $g^{(2)}$ (results of the Hong–Ou–Mandel experiment) between a read-out field and an entanglement-probe pulse as a function of their detuning. The orange line shows a Gaussian fit and the black dashed line indicates the thermal-coherent interference limit (see Supplementary Information for more details). **c**,**d**, Reconstructed density matrices of $|\Psi^+_{pp}\rangle$ (**c**) and $|\Psi^-_{pp}\rangle$ (**d**) after 5 μs of storage. **f**,**g**, Reconstructed density matrices of $|\Psi^+_{pp}\rangle$ (**f**) and $|\Psi^-_{pp}\rangle$ (**g**) after 107 μs of storage. In the density matrix figures, blue bars are the tomography of the read-out fields and the transparent bars are the tomography of the atomic states by deducting the loss during retrieval and detection. **e**,**h**, Correlation measurements of $|\Psi^+_{PME}\rangle$ (**e**) and $|\Psi^-_{PME}\rangle$ (**h**). The blue and orange bars are the results for the 5-μs and 107-μs storage cases, respectively. The transparent bars are the theoretical correlators. The error bars represent one standard deviation.

from the write-out photons, which corresponds to a signal-to-noise ratio of 3 in the server node. The PME-state generation rate is 0.013 Hz and 0.0037 Hz for the two experiments, which is the product of the entanglement heralding rate, the retrieval efficiency and the average photon number of the entanglement-probe pulse.

Concurrent entanglement generation in the network

Now we complete the network architecture by including the third quantum node, Charlie, and concurrently generate entanglement $|\Psi^{\pm}\rangle_{AB}$, $|\Psi^{\pm}\rangle_{BC}$ and $|\Psi^{\pm}\rangle_{AC}$ on three links, Alice–Bob, Bob–Charlie and Alice–Charlie, respectively. To this end, the server node is equipped with a multi-input–two-output optical switch and assigns two of the three users to the detection upon request. In our demonstration, we assign a 5.8-s timeslot for each pair of users and dynamically switch user pairs according to a quantum random number generator (QRNG), simulating unknown requests in real-world applications. As different links are frequently switched, a 'hot swapping' feature is crucial, that is, the entangling conditions are met immediately after switching. In our architecture, the phase stabilization is executed for every entanglement trial and is unaffected by switching. The good laser stability guarantees an ignorable relative frequency drift although a one-third effective calibration time is assigned for each pair of nodes. Furthermore, we track the polarization drift of each fibre and immediately apply the compensation (see ref. 32) during switching.

We first observe the local manipulation of non-local states. For instance, when applying a unitary operation locally at one of the quantum nodes (for example, Charlie), its relevant non-local states ($|\Psi^{\pm}\rangle_{AC}$ and $|\Psi^{\pm}\rangle_{BC}$) change in form while the entanglement is preserved. The irrelevant non-local states $|\Psi^{\pm}\rangle_{AB}$ remain unchanged. In practice, we vary the phase θ at Charlie and measure the $\langle XX\rangle$ correlation of each pair of entanglement. As shown in Fig. 4a,b, we observe sinusoidal oscillations in the expected pairs $|\Psi^{\pm}\rangle_{BC}$ and $|\Psi^{\pm}\rangle_{AC}$, while $|\Psi^{\pm}\rangle_{AB}$

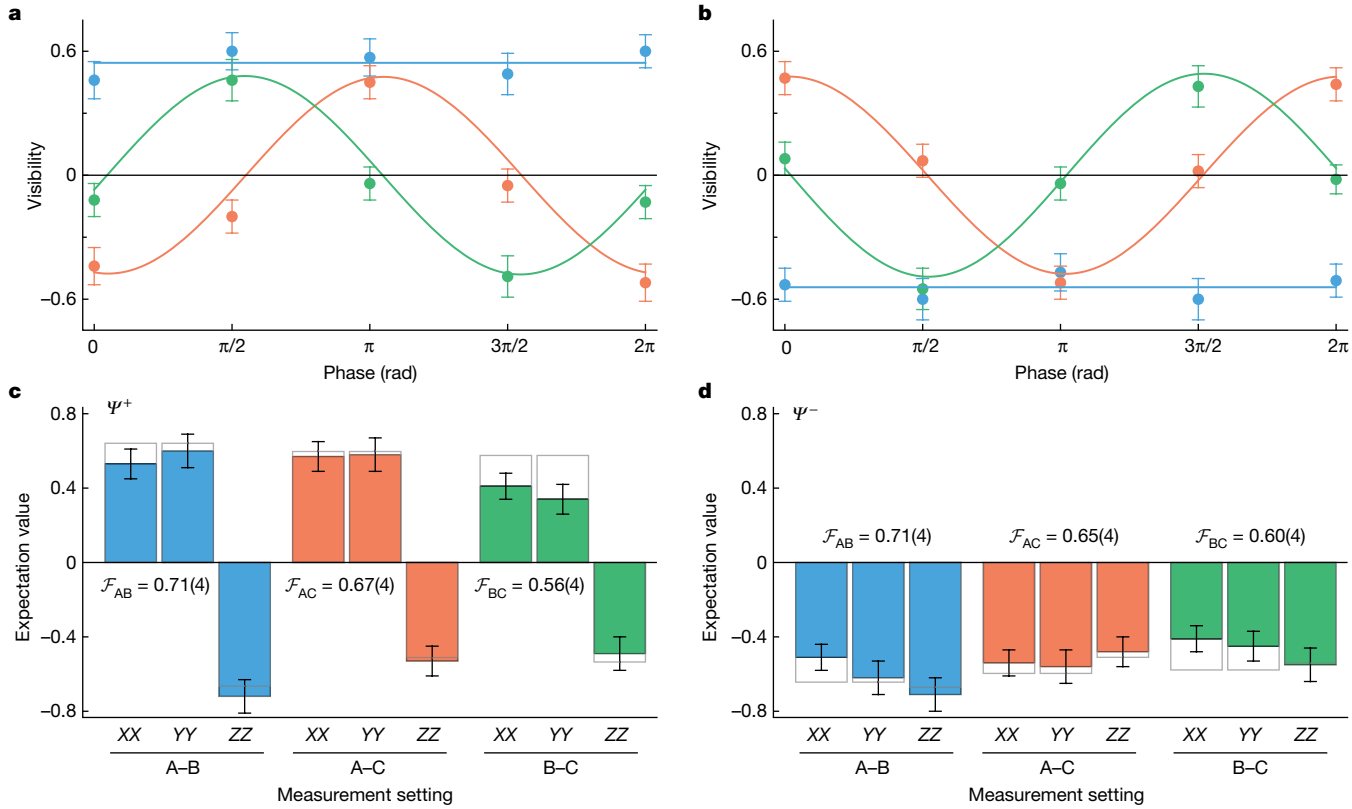

Fig. 4 | Concurrent entanglement generation in the network. a,**b**, Measured correlation $\langle XX\rangle$ of $|\Psi^+\rangle$ (**a**) and $|\Psi^-\rangle$ (**b**) on three links when changing the phase θ at Charlie. Blue, orange and green data points refer to the results of the Alice–Bob, Alice–Charlie and Bob–Charlie links, respectively. The curves show the sinusoidal or the linear fit of data with corresponding colours. **c**,**d**, Correlation measurement of $|\Psi^+_{PME}\rangle$ (**c**) and $|\Psi^-_{PME}\rangle$ (**d**) on three links. The colour code is the same as in **a** and **b**. The transparent bars refer to the theoretical correlators. The error bars represent one standard deviation.

contributes a constant in this measurement. A π/2 delay between the oscillations of $|\Psi^{\pm}\rangle_{BC}$ and $|\Psi^{\pm}\rangle_{AC}$ arises from the phase-stabilization mechanism (Supplementary Information).

In the end, we characterize the generated remote entangled states on three links in the delayed-choice fashion. Table 1 summarizes the concurrence results $\mathcal{C}$ and $\tilde{\mathcal{C}}$ and Fig. 4c,d shows the correlation measurement results of the PME states and gives the fidelities as well. For all three links, we find $\mathcal{C} > 0$ to confirm the presence of atomic entanglement and $\mathcal{F} > 0.5$ indicates the entanglement in the corresponding PME state. The entangled states between Alice and Bob are comparable to that generated in the fixed connection case, indicating no extra decoherence being introduced in the switching process. The lower entanglement quality in other links arises from experimental imperfections (Supplementary Information). The entangling rates of all three links are roughly one-third of that measured in the fixed connection case, as expected. Some simple upgrades to the server node will immediately improve the networking performance, such as parallel (rather than concurrent) creation of multiple entanglement pairs with the help of wavelength division multiplexing technique[40] and genuine three-body entanglement creation using a modified interferometer[21,41,42].

Table 1 | Summary of the concurrence results in the concurrent entanglement generation experiment

		Alice–Bob	Alice–Charlie	Bob–Charlie
$\mathcal{C}$	$\|\Psi^+\rangle$	0.086(14)	0.074(14)	0.032(12)
	$\|\Psi^-\rangle$	0.086(14)	0.063(13)	0.048(13)
$\tilde{\mathcal{C}}$	$\|\Psi^+\rangle$	0.38(5)	0.35(5)	0.17(5)
	$\|\Psi^-\rangle$	0.38(5)	0.30(5)	0.23(5)

Discussion and outlook

In this work, we present the implementation of a metropolitan-area entanglement-based quantum network. With this facility, we have successfully demonstrated the heralded generation of remote entanglement between two quantum nodes separated by 12.5 km and stored it longer than the round-trip communication time. We also showed the concurrent generation of multiple entanglement pairs within the network. The high entangling rate in our network is enabled by the single-photon scheme[34], which provides an entangling rate proportional to $\chi\sqrt{\eta}$ (χ is the single-photon probability and η is the channel transmittance), superior to that of the two-photon scheme[43] ($\chi^2\eta$) and the serial-network scheme[44] ($\chi\eta$). We overcome the technical challenges in the single-photon scheme using a series of methods, two of which are crucial. First, the remote phase stabilization guarantees the basis to implement the single-photon scheme. In addition, it provides a flexible and scalable network infrastructure that can accommodate more quantum nodes within the metropolitan area. Second, the weak-field method simplifies the verification of remote Fock-basis entanglement. It removes the necessity to interfere two remote Fock-basis photons, and instead requires only local linear optics operations and measurements. Moreover, using this method, one can effectively convert Fock-basis entanglement to the polarization maximally entangled state, making entanglement-based communication within reach. These methods promise the scalability of our network on larger scales and more complex topologies. Adapting these methods to other physical platforms will accelerate their networking process.

Further advances of the network performance will happen in four main aspects, increasing the entangling rate by shifting the wavelength

to telecom C band[27,31] and by adapting multiplexed atomic quantum memories[45]; decreasing the entanglement infidelity by suppressing unwanted higher-order atomic excitations with the help of a Rydberg blockade mechanism[38,46]; realizing a better entanglement verification by filtering out the vacuum components in the remote entangled state[10,34] or by using nonlinear atomic-state detection techniques[36,47]; and prolonging the entanglement storage time to the second scale by further limiting atomic thermal motion with an optical lattice technique[48]. With these improvements, we expect to realize quantum repeater links on an intercity scale and merge several metropolitan-area quantum networks into a wide-area complex network, as envisaged in Fig. 1a.

Online content

Any methods, additional references, Nature Portfolio reporting summaries, source data, extended data, supplementary information, acknowledgements, peer review information; details of author contributions and competing interests; and statements of data and code availability are available at https://doi.org/10.1038/s41586-024-07308-0.

1. Kimble, H. J. The quantum internet. *Nature* **453**, 1023–1030 (2008).
2. Wehner, S., Elkouss, D. & Hanson, R. Quantum internet: a vision for the road ahead. *Science* **362**, eaam9288 (2018).
3. Sangouard, N., Simon, C., de Riedmatten, H. & Gisin, N. Quantum repeaters based on atomic ensembles and linear optics. *Rev. Mod. Phys.* **83**, 33–80 (2011).
4. Gisin, N., Ribordy, G., Tittel, W. & Zbinden, H. Quantum cryptography. *Rev. Mod. Phys.* **74**, 145–195 (2002).
5. Jiang, L., Taylor, J., Sørensen, A. & Lukin, M. Distributed quantum computation based on small quantum registers. *Phys. Rev. A* **76**, 062323 (2007).
6. Gottesman, D., Jennewein, T. & Croke, S. Longer-baseline telescopes using quantum repeaters. *Phys. Rev. Lett.* **109**, 070503 (2012).
7. Kómár, P. et al. A quantum network of clocks. *Nat. Phys.* **10**, 582–587 (2014).
8. Briegel, H.-J., Dür, W., Cirac, J. I. & Zoller, P. Quantum repeaters: the role of imperfect local operations in quantum communication. *Phys. Rev. Lett.* **81**, 5932–5935 (1998).
9. Chou, C. W. et al. Measurement-induced entanglement for excitation stored in remote atomic ensembles. *Nature* **438**, 828–832 (2005).
10. Chou, C.-W. et al. Functional quantum nodes for entanglement distribution over scalable quantum networks. *Science* **316**, 1316–1320 (2007).
11. Yuan, Z.-S. et al. Experimental demonstration of a BDCZ quantum repeater node. *Nature* **454**, 1098–1101 (2008).
12. Hofmann, J. et al. Heralded entanglement between widely separated atoms. *Science* **337**, 72–75 (2012).
13. Bernien, H. et al. Heralded entanglement between solid-state qubits separated by three metres. *Nature* **497**, 86–90 (2013).
14. Hensen, B. et al. Loophole-free Bell inequality violation using electron spins separated by 1.3 kilometres. *Nature* **526**, 682–686 (2015).
15. Humphreys, P. C. et al. Deterministic delivery of remote entanglement on a quantum network. *Nature* **558**, 268–273 (2018).
16. Moehring, D. L. et al. Entanglement of single-atom quantum bits at a distance. *Nature* **449**, 68–71 (2007).
17. Lago-Rivera, D., Grandi, S., Rakonjac, J. V., Seri, A. & de Riedmatten, H. Telecom-heralded entanglement between multimode solid-state quantum memories. *Nature* **594**, 37–40 (2021).
18. Liu, X. et al. Heralded entanglement distribution between two absorptive quantum memories. *Nature* **594**, 41–45 (2021).
19. Delteil, A. et al. Generation of heralded entanglement between distant hole spins. *Nat. Phys.* **12**, 218–223 (2016).
20. Stockill, R. et al. Phase-tuned entangled state generation between distant spin qubits. *Phys. Rev. Lett.* **119**, 010503 (2017).
21. Jing, B. et al. Entanglement of three quantum memories via interference of three single photons. *Nat. Photon.* **13**, 210–213 (2019).
22. Pompili, M. et al. Realization of a multinode quantum network of remote solid-state qubits. *Science* **372**, 259–264 (2021).
23. Hermans, S. L. N. et al. Qubit teleportation between non-neighbouring nodes in a quantum network. *Nature* **605**, 663–668 (2022).
24. Kumar, P. Quantum frequency conversion. *Opt. Lett.* **15**, 1476–1478 (1990).
25. Bock, M. et al. High-fidelity entanglement between a trapped ion and a telecom photon via quantum frequency conversion. *Nat. Commun.* **9**, 1998 (2018).
26. Ikuta, R. et al. Polarization insensitive frequency conversion for an atom–photon entanglement distribution via a telecom network. *Nat. Commun.* **9**, 1997 (2018).
27. Van Leent, T. et al. Long-distance distribution of atom–photon entanglement at telecom wavelength. *Phys. Rev. Lett.* **124**, 010510 (2020).
28. Tchebotareva, A. et al. Entanglement between a diamond spin qubit and a photonic time-bin qubit at telecom wavelength. *Phys. Rev. Lett.* **123**, 063601 (2019).
29. Krutyanskiy, V. et al. Light–matter entanglement over 50 km of optical fibre. *npj Quantum Inf.* **5**, 72 (2019).
30. Luo, X.-Y. et al. Postselected entanglement between two atomic ensembles separated by 12.5 km. *Phys. Rev. Lett.* **129**, 050503 (2022).
31. van Leent, T. et al. Entangling single atoms over 33 km telecom fibre. *Nature* **607**, 69–73 (2022).
32. Yu, Y. et al. Entanglement of two quantum memories via fibres over dozens of kilometres. *Nature* **578**, 240–245 (2020).
33. Bao, X.-H. et al. Efficient and long-lived quantum memory with cold atoms inside a ring cavity. *Nat. Phys.* **8**, 517–521 (2012).
34. Duan, L.-M., Lukin, M. D., Cirac, J. I. & Zoller, P. Long-distance quantum communication with atomic ensembles and linear optics. *Nature* **414**, 413–418 (2001).
35. Zhou, L., Lin, J., Jing, Y. & Yuan, Z. Twin-field quantum key distribution without optical frequency dissemination. *Nat. Commun.* **14**, 928 (2023).
36. Yang, C.-W. et al. Deterministic measurement of a Rydberg superatom qubit via cavity-enhanced single-photon emission. *Optica* **9**, 853–858 (2022).
37. Tan, S. M., Walls, D. F. & Collett, M. J. Nonlocality of a single photon. *Phys. Rev. Lett.* **66**, 252–255 (1991).
38. Li, L., Dudin, Y. O. & Kuzmich, A. Entanglement between light and an optical atomic excitation. *Nature* **498**, 466–469 (2013).
39. Ma, X.-s et al. Experimental delayed-choice entanglement swapping. *Nat. Phys.* **8**, 479–484 (2012).
40. Wengerowsky, S., Joshi, S. K., Steinlechner, F., Hübel, H. & Ursin, R. An entanglement-based wavelength-multiplexed quantum communication network. *Nature* **564**, 225–228 (2018).
41. Choi, K. S., Goban, A., Papp, S. B., Van Enk, S. J. & Kimble, H. J. Entanglement of spin waves among four quantum memories. *Nature* **468**, 412–416 (2010).
42. Dür, W., Vidal, G. & Cirac, J. I. Three qubits can be entangled in two inequivalent ways. *Phys. Rev. A* **62**, 062314 (2000).
43. Barrett, S. D. & Kok, P. Efficient high-fidelity quantum computation using matter qubits and linear optics. *Phys. Rev. A* **71**, 060310 (2005).
44. van Loock, P. et al. Hybrid quantum repeater using bright coherent light. *Phys. Rev. Lett.* **96**, 240501 (2006).
45. Collins, O. A., Jenkins, S. D., Kuzmich, A. & Kennedy, T. A. B. Multiplexed memory-insensitive quantum repeaters. *Phys. Rev. Lett.* **98**, 060502 (2007).
46. Sun, P.-F. et al. Deterministic time-bin entanglement between a single photon and an atomic ensemble. *Phys. Rev. Lett.* **128**, 060502 (2022).
47. Xu, W. et al. Fast preparation and detection of a Rydberg qubit using atomic ensembles. *Phys. Rev. Lett.* **127**, 050501 (2021).
48. Wang, X.-J. et al. Cavity-enhanced atom-photon entanglement with subsecond lifetime. *Phys. Rev. Lett.* **126**, 090501 (2021).

Publisher's note Springer Nature remains neutral with regard to jurisdictional claims in published maps and institutional affiliations.

Springer Nature or its licensor (e.g. a society or other partner) holds exclusive rights to this article under a publishing agreement with the author(s) or other rightsholder(s); author self-archiving of the accepted manuscript version of this article is solely governed by the terms of such publishing agreement and applicable law.

© The Author(s), under exclusive licence to Springer Nature Limited 2024

Data availability

Source data for the plots is archived on Zenodo at https://doi.org/10.5281/zenodo.8149009 (ref. 49).

49. Liu, J.-L. et al. Data for "Creation of memory–memory entanglement in a metropolitan quantum network". *Zenodo* https://doi.org/10.5281/zenodo.8149009 (2023).

Acknowledgements We acknowledge QuantumCTek for the allocation of node Bob, and Hefei Institutes of Physical Science for the allocation of node Charlie. This research was supported by the Innovation Program for Quantum Science and Technology (no. 2021ZD0301104), National Key R&D Program of China (no. 2020YFA0309804), National Natural Science Foundation of China (no. T2125010), Anhui Initiative in Quantum Information Technologies, and the Strategic Priority Research Program of the Chinese Academy of Sciences (no. XDB35000000).

Author contributions X.-H.B. and J.-W.P. conceived and designed the research. J.-L.L., X.-Y.L., Y.Y., C.-Y.W., B.W., Z.Y. and D.T. performed the experiment. Y.H., J.-W.J. and X.J. developed the phase feedback electronics. M.-Y.Z., X.-P.X. and Q.Z. built the QFC modules. B.Y., X.-B.L. and Q.-H.M. made a pump laser for the QFC. J.Z. contributed silicon single-photon detectors. J.-L.L., X.-Y.L., Y.Y., X.-H.B. and J.-W.P. analysed the data and wrote the paper with input from all other authors.

Competing interests The authors declare no competing interests.

Additional information

Supplementary information The online version contains supplementary material available at https://doi.org/10.1038/s41586-024-07308-0.

Correspondence and requests for materials should be addressed to Xiao-Hui Bao or Jian-Wei Pan.

Peer review information *Nature* thanks Simon Baier, Rikizo Ikuta and Michał Parniak for their contribution to the peer review of this work.

Reprints and permissions information is available at http://www.nature.com/reprints.